HD152843 b & c: the masses and orbital periods of a sub-Neptune and a superpuff Neptune

B. A. Nicholson [1,2][*] S. Aigrain,[2] N. L. Eisner [3,4] M. Cretignier,[2] O. Barragán,[2] L. Kaye,[2]
J. Taylor [2] J. Owen [5,6] A. Mortier [7] L. Affer,[8] W. Boschin,[9,10,11] L. A. Buchhave,[12]
A. Collier Cameron [13] M. Damasso,[14] L. Di Fabrizio,[9] V. DiTomasso,[15] X. Dumusque,[16] A. Ghedina,[9]
D. W. Latham,[15] M. López-Morales,[15] V. Lorenzi,[9,10] A. F. Martínez Fiorenzano,[9] E. Molinari,[17]
M. Pedani,[9] M. Pinamonti,[14] K. Rice[18,19] and A. Sozzetti[14]

[1]*Centre for Astrophysics, University of Southern Queensland, Toowoomba, QLD 4350, Australia*
[2]*Sub-department of Astrophysics, University of Oxford, Keble Rd, Oxford OX13RH, UK*
[3]*Center for Computational Astrophysics, Flatiron Institute, 162 Fifth Avenue, New York, NY 10010, USA*
[4]*Department of Astrophysical Sciences, Princeton University, Princeton, NJ 08544, USA*
[5]*Astrophysics Group, Department of Physics, Imperial College London, Prince Consort Rd, London SW7 2AZ, UK*
[6]*Department of Earth, Planetary, and Space Sciences, University of California, Los Angeles, CA 90095, USA*
[7]*School of Physics & Astronomy, University of Birmingham, Edgbaston, Birmingham B15 2TT, UK*
[8]*INAF - Osservatorio Astronomico di Palermo, Piazza del Parlamento 1, I-90134 Palermo, Italy*
[9]*Fundacion Galileo Galilei INAF (Telescopio Nazionale Galilei), Rambla Jose Ana Fernandez Perez 7, E-38712 Brenã Baja (La Palma), Canary Islands, Spain*
[10]*Instituto de Astrofisica de Canarias (IAC), C/Via Lactea s/n, E-38205 La Laguna (Tenerife), Canary Islands, Spain*
[11]*Departamento de Astrofisica, Univ. de La Laguna, Av. del Astrofisico Francisco Sanchez s/n, E-38205 La Laguna (Tenerife), Canary Islands, Spain*
[12]*DTU Space, Technical University of Denmark, Elektrovej 328, DK-2800 Kgs. Lyngby, Denmark*
[13]*Centre for Exoplanet Science / SUPA, School of Physics & Astronomy,University of St Andrews, North Haugh St Andrews, Fife KY16 9SS, UK*
[14]*INAF - Osservatorio Astrofisico di Torino, Strada Osservatorio, 20, I-10025 Pino Torinese (TO), Italy*
[15]*Center for Astrophysics | Harvard & Smithsonian, 60 Garden Street, Cambridge, MA 02138, USA*
[16]*Observatoire de Geneve, 51 Chemin Pegasi, CH-1290 Versoix, Switzerland*
[17]*INAF - Osservatorio Astronomico di Brera & REM via Bianchi 46, I-23807 Merate (LC), Italy*
[18]*Institute for Astronomy, University of Edinburgh, Royal Observatory, Blackford Hill, Edinburgh EH9 3HJ, UK*
[19]*Centre for Exoplanet Science, University of Edinburgh, Edinburgh EH9 3HJ, UK*

ABSTRACT

We present the characterization of the two transiting planets around HD 152843 (TOI 2319, TIC 349488688) using an intensive campaign of HARPS-N radial velocities, and two sectors of *TESS* data. These data reveal a unique and fascinating system: HD 152843 b and c have near equal masses of around 9 $M_\oplus$ but differing radii of 3.05 ± 0.11 $R_\oplus$ and $5.94^{+0.18}_{-0.16}$ $R_\oplus$, respectively, and orbital periods of $11.62071^{+9.6e-05}_{-0.000106}$ and $19.502104^{+7.4e-05}_{-8.5e-05}$ d. This indicates that HD 152843 c is in the lowest fifth-percentile in density of the known exoplanet population, and has the longest orbital period among these low-density planets. Further, HD 152843 c's radius places it in the 'Saturn valley', the observed lack of planets larger than Neptune, but smaller than Saturn. The orbital periods of these planets indicate they are near a 5 : 3 mean motion resonance, indicating the possibility of transit timing variations, and hints at the possibility of interaction with a third planet at some point in the evolution of this system. Further, the brightness of the host star and the low density of HD 152843 c make it a key target for atmospheric characterization.

Key words: exoplanets – stars: individual: TIC 349488688, HD 152843.

1 INTRODUCTION

Transiting exoplanets with well-characterized orbits, masses, and radii are highly valuable for detailed studies of planetary astrophysics. Even more valuable are such systems hosting multiple transiting planets – they provide robust constraints on planet formation and evolution models since these models must be able to explain the properties of all planets in the system.

In the era of large-scale stellar photometric surveys searching for transiting planets, many multiple transiting planet systems have been found. However, many of these systems have been found around stars for which the follow-up radial velocity observations necessary for measuring their masses and full orbital characteristics are challenging: faint stars cannot provide the signal required for high-resolution spectroscopy, and the signal of a planet

[*] E-mail: belinda.nicholson@unisq.edu.au

that is easy to detect in transit can be small in radial velocity (RV).

Eisner et al. (2021b) (hereafter E21) presented the discovery of a system ideal for precise characterization: two planets orbiting HD 152843, a bright (V = 8.85 mag), solar-type (T$_{eff}$ = 6310 ± 100 K), main-sequence star. Transits of these planets, two of planet b and one of planet c, were seen in Sector 25 of NASA's *Transiting Exoplanet Survey Satellite* (*TESS*, Ricker et al. 2015) primary mission and flagged by citizen scientists through the Planet Hunters *TESS* project (Eisner et al. 2021a). E21 made robust radii measurements of both planets, measured the orbital period of planet b, and placed constraints on the orbital period of planet c given its transit duration and the gaps and time span of the *TESS* data. Some radial velocity data were taken to validate the system, but these were not sufficient to provide robust mass measurements for either planet.

Even with this limited information, HD 152843 stood out as an intriguing system: planet c lies in a sparsely populated region of the radius–period diagram, in the 'gap' between Neptunes and Saturns/Jupiters ($5 < R_p < 8$ $R_\oplus$, see fig. 9 of E21). This region contains both relatively high-density, warm sub-Saturns with a significant solid core, and extremely low-density 'superpuffs' that have densities of the order of ∼0.1 g cm^{-3} (Jontof-Hutter 2019). The former case represents planets that have crossed the core mass threshold for runaway accretion towards a Jupiter-size, but have failed to do so due to the environment of the disc (see e.g. Helled 2023). The nature and origins of the latter 'superpuff' case are still uncertain. One possible scenario is stellar radiation creating high-altitude hazes that increase opacity out to larger planetary radii, making the planet appear larger than it would if its atmosphere was free of aerosols (Lammer et al. 2016; Gao & Zhang 2020). Another possible scenario is that superpuff planets have additional sources of heating (i.e. tidal heating), which give rise to a thermally inflated radius (Millholland, Petigura & Batygin 2020).

Planet c is also intriguing as it resides in a system alongside a relatively 'normal' sub-Neptune, planet b. Comparing and contrasting the properties of the two planets could yield useful insights into the processes that sculpt the 'sub-Saturn valley' and/or the origin of superpuffs. However, precise constraints on the period and mass of planet c are needed in order to constrain theoretical models of how these planets are formed.

This paper presents the precise masses and orbital parameters of HD 152843 b and c, achieved through intensive RV monitoring with the HARPS-N instrument through the HARPS-N GTO program, and additional *TESS* data. In Section 2, we detail these observations and data reduction and processing steps. Section 3 describes the properties and parameters of the host star used to interpret our data, and explores any signs of stellar activity in the HARPS-N spectra and radial velocities. We show the results of the joint modelling of the transit and radial velocity data in Section 4 to obtain the orbital periods, masses, and radii for both planets. With these parameters established, Section 5 discusses the implications of these on scenarios of formation and evolution of this system. We summarize and conclude our findings in Section 6.

2 OBSERVATIONS

This work uses multiyear, high-precision, space-based photometry and ground-based radial velocity observation, spanning just over 3 yr in both cases. While the observations from the first season were discussed in the discovery paper (E21), in this work, we re-analysed the full light curve and RV data sets and thus describe both in their entirety.

2.1 *TESS* photometry

TESS first observed HD 152843 in Sector 25 of its primary mission, covering two transits of HD 152843 b and one of c (E21). HD 152843 was re-observed by *TESS* in Sector 52 of its extended mission, during which two additional transits of planet b, and one of c were observed.

In both sectors, the spacecraft obtained images at a cadence of 2 s, which were combined onboard the satellite into 2 min cadence data products. These were processed and reduced by the Science Processing Operations Center (SPOC; Jenkins et al. 2016). Throughout this work, we use the pre-search data conditioning simple aperture photometry (PDC) light curve from the SPOC pipeline as our starting point. Sector 52 was affected by significant levels of Earth-shine (Fausnaugh et al. 2022), which saturates portions of the detector and makes some sections of the light curve unusable, while introducing additional systematics in the rest. Parts of the light curve that were affected by intermediate levels of Earth-shine are included in the simple aperture photometry (SAP) light curve, but not in the PDC version. The second transit of HD 152843 c falls within one of these segments. Since this transit is critical to pin down the period of HD 152843 c, we processed the relevant section of the SAP light curve ourselves.

To process the Sector 52 SAP light curve for the transit of planet c, we used the LIGHTKURVE python package (Lightkurve Collaboration 2018) to subtract the background flux, and correct for crowding and aperture losses (as is normally done as part of the PDC pipeline). To ascertain the potential impact of *TESS* systematics on the light curve around the transit of HD 152843 c, we modelled the systematics using the co-trending basis vectors (CBVs). These are computed by the PDC pipeline, and so were not available for the time-range of planet c's transit, but modelling the CBVs that were available allowed us to check that there were no large systematics around the transit, which would alter its shape or measured depth.

The full *TESS* light curve is shown in Fig. 1, normalized to its median in each sector. The top panel shows Sector 25, including the two transits of HD 152843 b (blue shading) and one transit of HD 152843 c (orange shading), which were already analysed by E21. This light curve has a total of 17 245 data points between 2020 May 14 and June 8, with a mean uncertainty of 5.0 parts per thousand (ppt). The bottom panel shows the PDC light curve for Sector 52, which has a total of 10 843 observations between 2022 May 19 and June 12 with an average uncertainty of 4.5 ppt, and contains two additional transits of HD 152843 b. The middle panel shows the SAP light curve for Sector 52, including the section around the transit of HD 152843 c, which was missing from the PDC light curve and has an additional 590 data points with an average uncertainty of 6.0 ppt. The ∼ 1 d data gap in the middle of each sector corresponds to the time taken for the spacecraft to point its antenna towards Earth (at the periapse of *TESS*'s orbit), to send data to Earth and re-point. Additional data gaps in Sector 52 are caused by Earth-shine.

To prepare the light curve for analysis, we select segments of the light curve lasting 0.5 d around each transit. We used the PDC light curve wherever available, since that is expected to be the most reliable, and used our processing of the SAP light curve only for the second transit of planet c. Due to the gap in the *TESS* data and significant Earth-shine prior to the transit of HD 152843 c, the out-of-transit baseline prior to this transit is shorter than the 0.5 d cut-off. We normalize the baseline flux around each transit by fitting a first-order polynomial to the out-of-transit flux and dividing by the result. This process is illustrated in Fig. 2 for the second transit of planet c (Sector 52, SAP data). This is the transit with the steepest baseline
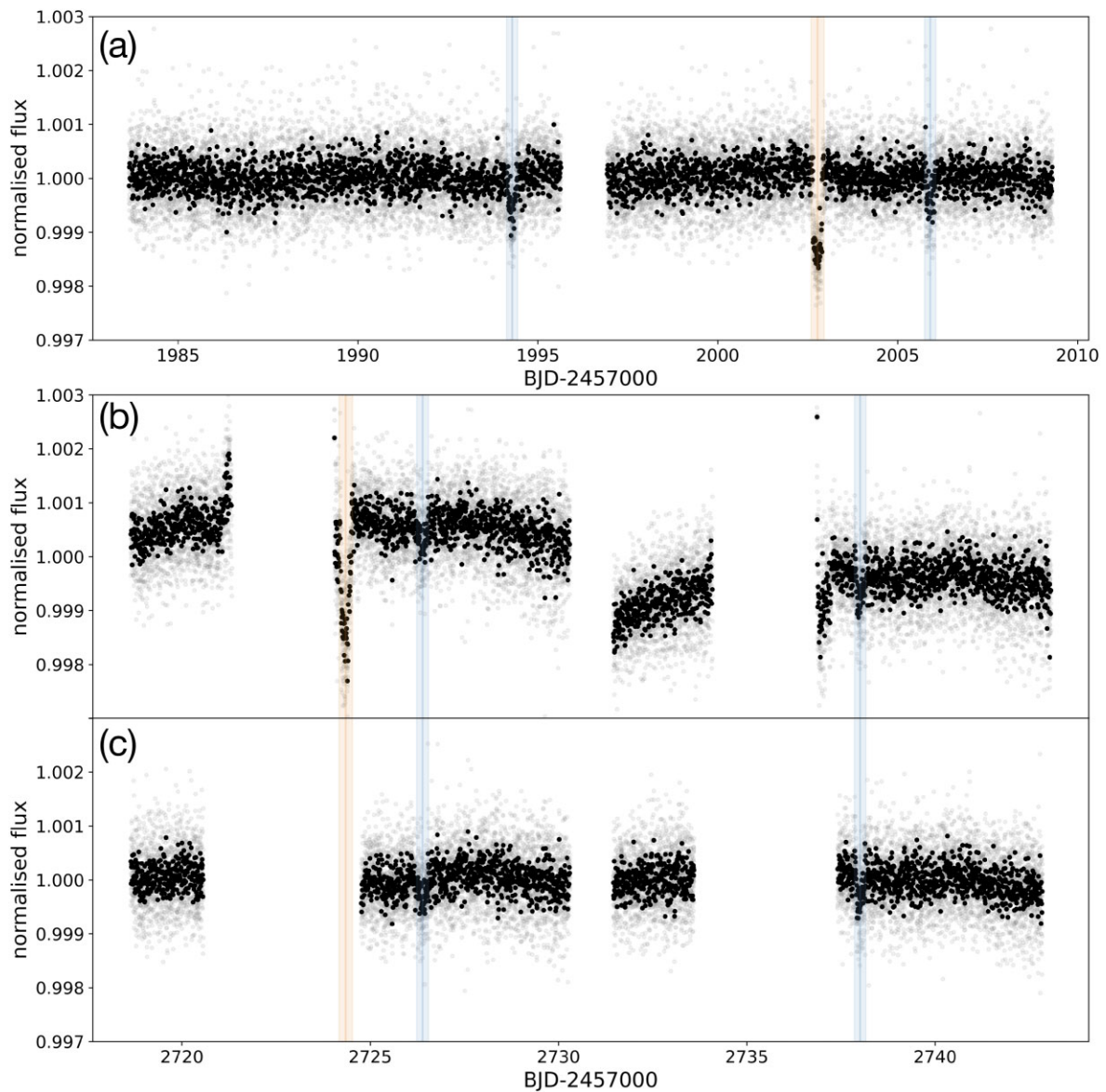
Figure 1. Normalized photometric *TESS* data for HD 152843. (a) Sector 25 PDC-SAP, (b) Sector 52 SAP, (c) Sector 52 PDC-SAP. In all panels, the grey points show the 2-min cadence data, the black points show the data binned to 10-min cadence, and the shaded blue and orange regions highlight transits of planets b and c, respectively.
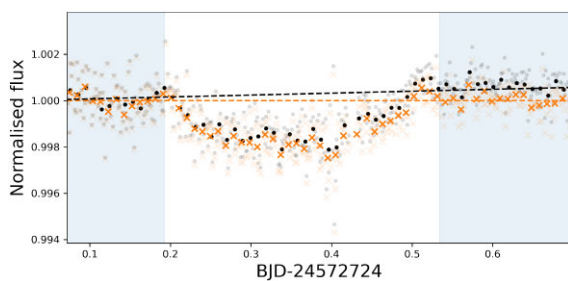

Figure 2. Fit to the out-of-transit baseline for the second transit of planet c (Sector 52, SAP data). The time-ranges used for the fit are indicated by the blue shaded areas. The input 2-min cadence data are shown by the grey dots and the resulting, normalized data by the faint orange crosses. The same data sets are also shown binned to 14-min cadence (black dots and orange crosses, respectively).

trend: the gradient of the light curve around the transit is significantly smaller for all the other transits, where we used the PDC data.

2.2 HARPS-N spectroscopy

We acquired high-resolution ($R \approx 115\,000$) spectra with the High Accuracy Radial velocity Planet Searcher in the Northern hemisphere (HARPS-N; Cosentino et al. 2012, 2014) spectrograph mounted at the 3.6-m Telescopio Nazionale Galileo in La Palma, Spain, via a Director's Discretionary Time program (ID: A41DDT4) and subsequently through the HARPSN-GTO program. We obtained 18 spectra between 2020 September 5 and November 11, 65 spectra between 2021 March 3 and September 23, and 87 spectra between 2022 February 4 and October 5. Most of exposures were at 900 s, with a handful of longer exposure (1x1800, 1x1500, and 4x1200 s) to compensate for poor conditions, and two aborted observations that have exposure times too short to be useful. The resulting mean signal-
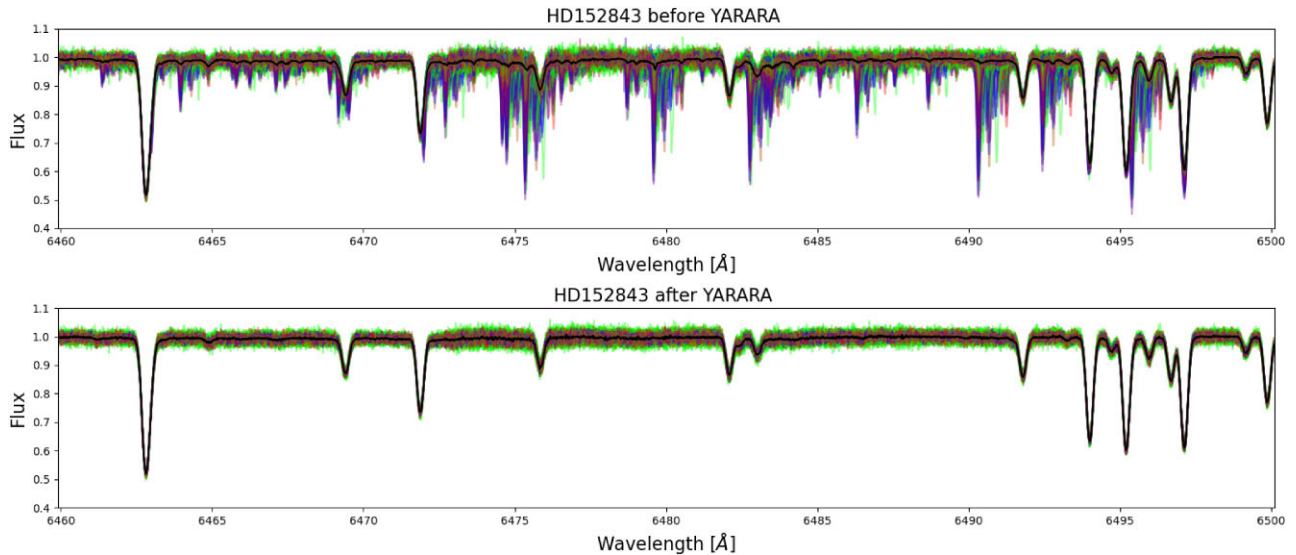
Figure 3. Correction of telluric lines by YARARA. The individual spectra are each plotted in a different colour before (top) and after (bottom) YARARA post-processing.

to-noise ratio (SNR) at 550 nm of the completed observations is 101. The wavelength solution was determined by simultaneous wavelength calibration with a Fabry–Perot etalon and nightly calibration frames with a Thorium–Argon lamp. The first season of observations, analysed by E21, was originally reduced using the standard HARPS DATA REDUCTION SOFTWARE (DRS version 3.7; Baranne et al. 1996), including RV extraction via cross-correlation with a G2 spectral template, yielding a mean RV uncertainty of $\sim 4.2\,\mathrm{m\,s^{-1}}$. In this work, all the observations were re-reduced using the more recent version 2.3.5 of the DRS (Dumusque et al. 2021), which has been shown to reduce systematics. In addition to calculating the radial velocities, the DRS also computes the moments and bisector span of the cross-correlation function (CCF), and an S-index and log R'_{HK} from the Ca II H&K lines as stellar activity indicators.

2.2.1 Post-processing and radial velocity determination with YARARA

For moderate rotators such as HD 152843 ($v \sin i_\star = 8.38 \pm 0.5\,\mathrm{km\,s^{-1}}$), the cross-correlation RV extraction process yields larger RV uncertainties than that for slower rotators, as the broadening of the spectral lines reduces the Doppler information content contained in the spectra. Furthermore, broader line profiles also increase the amount of heavily blended lines that are unsuitable for CCF extraction and should be avoided from the CCF mask. Last but not least, the DRS spectra used here contain residual instrumental and telluric signatures. All those considerations pushed us to perform a careful and attentive RV extraction for this target. We attempt to improve the accuracy of our RV estimates by post-processing the time-series of DRS-reduced 1D spectra using YARARA (Cretignier et al. 2021).

The post-processing begins from the 1D spectra produced by the official DRS (Dumusque et al. 2021). A subset of the observations (totalling 136) was selected, as YARARA requires a homogeneous data set of high SNR observations. Specifically, spectra with SNR< 75 were excluded, as were those corresponding to $\geq 3\sigma$ outliers in one of the CCF moments or the S-index produced by the DRS. These outliers typically indicate exposures that have been taken under sub-

optimal observing conditions (e.g. clouds or moonlight) or that have been reduced using non-standard calibration frames.

The remaining spectra were first continuum-normalized using a convex hull algorithm implemented in the PYTHON package RASSINE (Cretignier et al. 2020b), which has been shown to approximate the continuum at a precision compatible with the photon-noise of the observations. The continuum-normalized spectra were then median-combined to construct a master stellar spectrum, which was subtracted from the individual spectra. The matrix of residual spectra was then analysed to reveal and correct for flux systematics such as cosmic rays, tellurics, ghosts, interference patterns, and point spread function variations (Cretignier et al. 2021). YARARA can also correct stellar activity effects in the spectra, but this step was not performed here, since the star is not active (see Section 3.1). Even though the median SNR of the observations is only ~ 100, whereas the performance of YARARA is at its full potential when applied for bright targets (SNR>250), we still see a clear improvement in the spectra, as illustrated by Fig. 3 for a region contaminated by telluric lines.

The DRS usually computes a CCF using a generic line list, optimized for a broad spectral type class. As shown in Bourrier et al. (2021), this results in sub-optimal RV estimates, and improved RVs can be obtained by deriving a bespoke line list, tailored for the star's specific temperature and metallicity, from the spectra themselves following the method of Cretignier et al. (2020a). Here, we followed the same procedure except that we did not exclude lines contaminated by telluric lines, since those are now corrected by YARARA. Once the CCF is computed, the RV extraction proceeds by fitting a Gaussian to the CCF as in the standard DRS.

2.3 Final RVs and activity indicators

Table 1 summarizes the full set of observations of HD 152843 from HARPS-N. The full list is included as supplementary material to this paper. For the analysis that follows we use the YARARA radial velocities, and activity indicators. The median RV uncertainty and SNR of this final data set are 1.71 m s^{-1} and 108, respectively. For reference, the main pipeline radial velocities are included and a "Use Flag" column, where a vlaue of 1 indicates that observation is used

Table 1. Journal of observations of HD152843 taken with the HARPS-N instrument, including SNR calculated at 550 nm, standard pipeline (DRS) radial velocity measurements with uncertainties, as well as radial velocities and activity indicators computed by the YARARA pipeline for observations included in the analysis, indicated with 'Use Flag'=1. Some observations were excluded from the analysis ('Use Flag' = 0) due to low SNR (SNR < 75) or outliers rejection criterion (see the main text). The full table is provided in machine-readable format as supplementary material.

Time (BJD−2457000)	SNR	DRS RV (m s^{-1})	σ_{RV} (m s^{-1})	RV (m s^{-1})	σ_{RV} (m s^{-1})	YARARA log R'_{HK}	$\sigma_{\log R'_{HK}}$	Bis. Span	$\sigma_{Bis.Span}$	Use Flag 1 or 0
2098.3530	157	9872.394874	1.691244	2.575514	1.246248	−5.308577	0.452185	9.453929	2.245117	1
2102.3420	120	9863.510576	2.268848	−4.495355	1.467149	−5.329140	0.456954	−52.470551	3.909014	1
2104.3659	20	9869.671016	16.359800	NaN	NaN	NaN	NaN	NaN	NaN	0
2110.3261	87	9864.607312	3.144023	−4.607612	3.189392	−5.149874	0.463961	−2.009999	2.704267	1
2111.3796	100	9868.244643	2.712388	2.353805	1.714082	−5.748914	0.458733	129.392928	3.923864	1
2114.3398	67	9876.167603	4.003329	NaN	NaN	NaN	NaN	NaN	NaN	0
⋮	⋮	⋮	⋮	⋮	⋮	⋮	⋮	⋮	⋮	⋮

Table 2. Stellar parameters of HD152843 used for the analysis in this paper. Values are from E21, except where noted: $^{(a)}$ Bruntt et al. (2010).

Effective temperature T_{eff} (K)	6310 ± 100
Surface gravity $\log g_\star$ (cgs)	4.19 ± 0.03
$v \sin i_\star$ (km s^{-1})	8.38 ± 0.50
[M/H] (dex)	-0.22 ± 0.08
[Fe/H] (dex)	-0.16 ± 0.05
v_{mic} (km s^{-1})	1.66 ± 0.13
v_{mac} (km s^{-1})	$\sim 2^{(a)}$
Stellar mass $M_\star$ ($M_\odot$)	1.15 ± 0.04
Stellar radius $R_\star$ ($R_\odot$)	1.43 ± 0.02
Stellar density $\rho_\star$ ($\rho_\odot$)	0.40 ± 0.03
Star age (Gyr)	3.97 ± 0.75

Figure 4. Lomb–Scargle periodograms of the log R'_{HK} (blue), detrended FWHM (orange), and bisector span (BIS, green) stellar activity indicators. The 5 per cent FAP level for each periodogram is indicated by the horizontal dashed line of the same colour. The two vertical lines are the estimated periods of planet b (left) and planet c (right).

in this analysis. In addition to excluding poor SNR or incomplete observations, we also exclude observations taken between 2021 May 8 and 12 from the analysis, due to a known problem with the guiding camera on those nights (private communication, TNG). While the observations of HD 152843 are not visibly affected, standard stars observed on those nights display an offset in their RV measurements, which undermined our confidence in the RVs for our target on those dates.

3 PARAMETERS AND ACTIVITY OF THE HOST STAR

We use the fundamental stellar parameters determined by E21 using the first 18 HARPS-N spectra, which are summarized in Table 2. The uncertainties on those parameters are dominated by systematic rather than random errors, and therefore re-estimating the parameters using the more recent HARPS-N observations would not yield significantly different values.

Given the significantly larger number of spectra, we can however investigate the activity of the host star in more depth than was done by E21.

3.1 Activity analysis

Our log R'_{HK} values for HD 152843 have a roughly Gaussian distribution around a value of −5.25 with a standard deviation of 0.06, except for a single outlier at −5.70. These low values suggest that HD 152843 is a quiet star, and that activity is not expected to affect the RVs significantly.
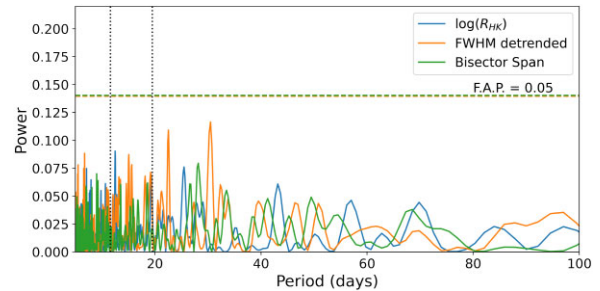
To double check this, we computed the Pearson correlation coefficient between the log R'_{HK} values and the RVs, which is 0.15, indicating very little correlation. We also computed Lomb–Scargle periodograms[1] of the chromospheric and CCF-based activity indicators, which are shown in Fig. 4. In the case of the CCF full width at half-maximum (FWHM), a small linear trend, which may be due to instrumental effects (focus drift) or secular changes in activity level (activity cycle), was subtracted before computing the periodogram. None of the indicators display peaks in their periodogram above the false alarm probability (FAP) threshold for significance of 5 per cent, and so show no significant periodicity. We place an upper limit on the stellar rotation period of ≈ 8.6 d based on the measured and estimated values of $v \sin i_\star$ and $R_\star$.

Finally, the light curve shown in Fig. 1 shows no signs of spot-induced variability. We therefore proceed to model the light curve and RVs without accounting for activity effects, which should be negligible compared to other sources of uncertainty.

4 JOINT MODELLING OF THE TRANSITS AND RVS

In this section, we describe the joint analysis of the *TESS* light curve and HARPS-N RVs to derive the parameters of the two planets.

---

[1]All Lomb–Scargle periodograms were computed in PYTHON using the TIME_SERIES.LOMBSCARGLE module of the ASTROPY package.
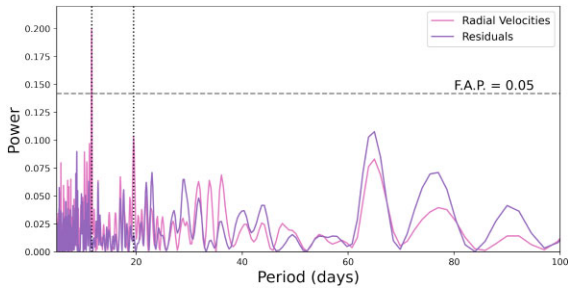
Figure 5. Lomb–Scargle periodograms of the raw RVs (pink) and the residuals of the two-planet fit (purple). The 5 per cent FAP level for each periodogram is indicated by the horizontal dashed line of the same colour. The two vertical lines are the estimated periods of planet b (left) and planet c (right).
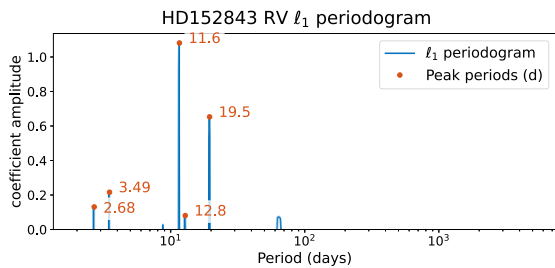

Figure 6. l_1 periodogram of the radial velocity time series of HD 152843. The two highest peaks have FAP values of 0.4 per cent and 2.1 per cent, and correspond to the orbital periods of planet b and c.

4.1 Periodogram analysis of the RVs

As a starting point of this analysis, we computed the Lomb–Scargle periodogram of the raw RVs to check if the RV signals of the two transiting planets are present in the RVs. This is shown as the pink line in Fig. 5. Peaks at the periods of both planets are clearly visible, though only the peak corresponding to planet b is statistically significant in this periodogram, which assumes the data consist of a single sinusoidal signal plus white noise. We therefore also computed the L1 periodogram (Hara et al. 2017), which is designed to search for signals from multiple planets at the same time. The periodogram is shown in Fig. 6. There are only two significant peaks, with (FAP < 5 per cent), corresponding to the periods of 11.62 and 19.50 d, which correspond to the measured and minimum possible orbital periods of planets b and c from *TESS* transit photometry.

Having established that the signals of both planets are present in the RVs, we now proceed to model the photometry and the RVs jointly.

4.2 Method and priors

The transit and RV data were jointly analysed using the open access PYTHON package PYANETI (Barragán, Gandolfi & Antoniciello 2019; Barragán et al. 2022). In brief, PYANETI fits the normalized transits using the model of Mandel & Agol (2002) with quadratic limb-darkening, and the RVs using Keplerian orbits, and samples the joint posterior over the parameters of the transit and RV fit using a Markov Chain Monte Carlo (MCMC) approach. All fitted parameters and priors used for the joint modelling are presented in Table 3. We also fit for the stellar density $\rho_\star$, and recover the scaled semimajor axis for each planet in the system using Kepler's third law. We use a Gaussian

prior on $\rho_\star$ based on the stellar mass and radius derived by E21 and reported in Table 3. We allowed for eccentric orbits for both planets, since their periods are too long to assume that the orbits have been tidally circularized.

For all our PYANETI runs, we sampled the parameter space using MCMC with 500 independent chains and created posterior distributions using 5000 iterations of converged chains with a thin factor of 10. Convergence was measured by the convergence test method of Gelman & Rubin (1992), where chains are considered converged when the scaled potential factor, which is function of the variance within and between chains, is less than 1.02 (Gelman et al. 2003). Overall, this resulted in 250 000 independent samples for each parameter.

4.3 Determining the period of planet c

The two transits we have observed of planet c are not sufficient to determine its orbital period, due to the large gap ($\sim$ 2 yr) between the two *TESS* sectors containing the transit events. We can, however, place constraints on what the possible periods might be from the *TESS* data, before refining this estimate using the RV time series. E21 constrained the minimum possible period to be 19.26 d from the data gaps and timing of the transit in the Sector 25 light curve, and this does not change with the additional *TESS* sector. They also derived an approximate upper limit on the period of $\sim$ 35 d based on the transit duration and stellar parameters. Within this broad range, P_c is constrained to lie within a number of narrow windows depending on the (integer) number of orbits separating the two observed transits.

The RVs can be used to discriminate between the different possible periods for planet c. Initially, we attempted a joint fit to the transits and RV data using a broad uniform prior on P_c, spanning 19.26–35 d. However, the posterior for P_c is highly multimodal within that range, with over a dozen sharp, narrow peaks. The MCMC algorithm used by PYANETI is designed to 'hone in' on the strongest mode(s) of the joint posterior distribution, and consequently fails to explore all of these peaks properly when given a broad uniform prior. Since we know the approximate location of the individual peaks, however, we can work around this problem by sampling them individually.

We therefore carried out separate PYANETI runs with a narrow, uniform prior on P_c around each possible period between 19.2 and 35 d given an integer number of orbits, with a width of 0.006 d. All the other parameter priors were as described in Table 3. The resulting log posterior distributions are plotted in Fig. 7. Because we used the same priors for each of these runs, changing only the location (but not the width) of the prior over P_c, the log posterior values for the samples from each run can be compared with each other directly. The marginal posterior distribution over P_c for each peak is well approximated by a Gaussian, and the shortest possible period of $P_c \sim 19.5$ d has a maximum in the log posterior that exceeds the other maxima by > 10. This indicates strong support for the shortest allowed period. Furthermore, this run is the one that yields the clearest detection of the RV signal of planet c (in terms of semi-amplitude over corresponding uncertainty), and is in agreement with the second most significant peak found in the $l1$ periodogram analysis of the RV data. We therefore use this value for P_c in our final analysis, described in the next section.

4.4 Final fit

Having ascertained that the shortest allowed period is the preferred one for planet c, we adopted the corresponding PYANETI run, which

Table 3. Parameters of the joint transit and RV fit.

Parameter	Prior[a]	Value[b]
Model parameters for HD 152843b		
Orbital period P_{orb} (d)	$\mathcal{U}[11.620, 11.622]$	$11.62071^{+9.6e-05}_{-0.000106}$
Transit epoch T_0 (BJD − 2457000)	$\mathcal{U}[1994.25, 1994.30]$	$1994.2853^{+0.0028}_{-0.003}$
Parametrization $e \sin \omega$	$\mathcal{U}[-1, 1]$	$-0.02^{+0.15}_{-0.16}$
Parametrization $e \cos \omega$	$\mathcal{U}[-1, 1]$	$0.06^{+0.19}_{-0.2}$
Scaled planet radius $R_p/R_\star$	$\mathcal{U}[0, 0.1]$	$0.01957^{+0.00062}_{-0.00063}$
Impact parameter, b	$\mathcal{U}[0, 1.1]$	$0.2^{+0.17}_{-0.14}$
Doppler semi-amplitude, K (m s^{-1})	$\mathcal{U}[0, 50]$	$2.53^{+0.44}_{-0.41}$
Model parameters for HD 152843c		
Orbital period P_{orb} (d)	$\mathcal{U}[19.499, 19.505]$	$19.502104^{+7.4e-05}_{-8.5e-05}$
Transit epoch T_0 (BJD − 2457000)	$\mathcal{U}[2002.76, 2002.78]$	$2002.7715^{+0.0016}_{-0.0015}$
Parametrization $e \sin \omega$	$\mathcal{U}[-1, 1]$	$0.05^{+0.16}_{-0.27}$
Parametrization $e \cos \omega$	$\mathcal{U}[-1, 1]$	$0.09^{+0.19}_{-0.23}$
Scaled planet radius $R_p/R_\star$	$\mathcal{U}[0, 0.1]$	$0.03804^{+0.00103}_{-0.00087}$
Impact parameter, b	$\mathcal{U}[0, 1.1]$	$0.3^{+0.18}_{-0.21}$
Doppler semi-amplitude, K (m s^{-1})	$\mathcal{U}[0, 50]$	$2.11^{+0.42}_{-0.42}$
Other parameters		
Stellar density $\rho_\star$ (g cm^{-3})	$\mathcal{N}[0.56, 0.04]$	$0.551^{+0.039}_{-0.04}$
Parametrized limb-darkening coefficient q_1 [c]	$\mathcal{U}[0, 1]$	$0.39^{+0.32}_{-0.15}$
Parametrized limb-darkening coefficient q_2 [c]	$\mathcal{U}[0, 1]$	$0.55^{+0.27}_{-0.24}$
Offset velocity HARPS-N (km s^{-1})	$\mathcal{U}[-0.50, 0.50]$	$0.00042^{+0.0003}_{-0.00029}$
Jitter HARPS-N (m s^{-1})	$\mathcal{U}[0, 100]$	$2.74^{+0.25}_{-0.23}$
Jitter *TESS* (ppm)	$\mathcal{U}[0, 500]$	240^{+130}_{-140}

Note. [a]$\mathcal{U}[a, b]$ refers to uniform priors between a and b, $\mathcal{N}[a, b]$ to Gaussian priors with mean a and standard deviation b. [b]The reported parameter values and errors are defined as the median and 68.3 per cent credible interval of the posterior distribution. [c]q_1 and q_2 parameters as in Kipping, Spiegel & Sasselov (2013)
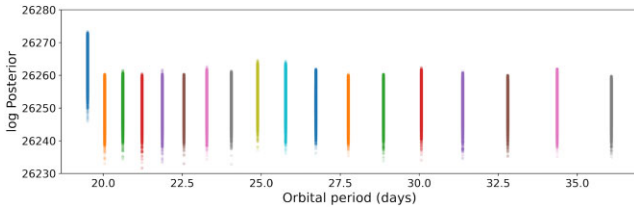
Figure 7. Log posterior for the period of HD 152843 c over the 19.26–35 d range allowed by the *TESS* light curve (see the text for details). The shortest period is clearly favoured.

set a uniform prior over P_c in the range 19.499 to 19.505 d, as the final one. The fitted parameters, extracted from the resulting posteriors, can be found in Table 3. The 1D and 2D posterior distributions for the orbital periods and semi-amplitudes of the two planets are shown in Fig. 8, showing that the posteriors for these parameters are approximately Gaussian and that the RV signals of both planets are detected at the $\sim 5\sigma$ level. The fits to the transits and RV data are shown in Figs 9 and 10, respectively. A figure showing the full set of 1D and 2D posterior distributions is provided in supplementary material.

The RV semi-amplitudes of both planets are non-zero at the $> 5\sigma$ level (see Fig. 8), hence they are both securely detected. The orbital eccentricity of both planets is consistent with zero. The posterior probability distributions over almost all the parameters, including

those not shown on Fig. 8, are approximately Gaussian and there are no significant correlations between parameters that might indicate a problem with the fit. The only exceptions are the impact parameters of the two planets and their eccentricity parameters $e \cos \omega$ and $e \sin \omega$, which do show some non-Gaussianity and mutual correlation, but this is entirely expected due to degeneracy between those parameter that cannot be fully resolved with these observations. The posterior distribution for the period of planet b (top left panel of Fig. 8) is somewhat non-Gaussian, which could indicate a tension between the different data sets used in the analysis, in particular between the two *TESS* sectors as these constrain the period of b more robustly than the RVs. We will return to this in Section 5.2 when discussing the system dynamics and the possibility of transit timing variations (TTVs).

The fit includes a 'jitter' term for each data type (photometry and RV), which is added in quadrature to the formal uncertainties. The photometric jitter term (285 ppm) was found to be significantly smaller than the median photometric uncertainty (484 ppm), indicating a good fit. The best-fitting RV jitter was 2.9 m s^{-1}, compared to a median formal RV uncertainty of 1.7 m s^{-1}. This indicates either that the formal uncertainties were slightly underestimated, or that there is an additional source of uncorrelated or correlated signal, such as stellar phenomena (e.g. granulation), instrumental changes, or additional planet signals, which are not accounted for by our model. This explains the comparatively large number of observations that were required to detect the RV signals of both planets to better than
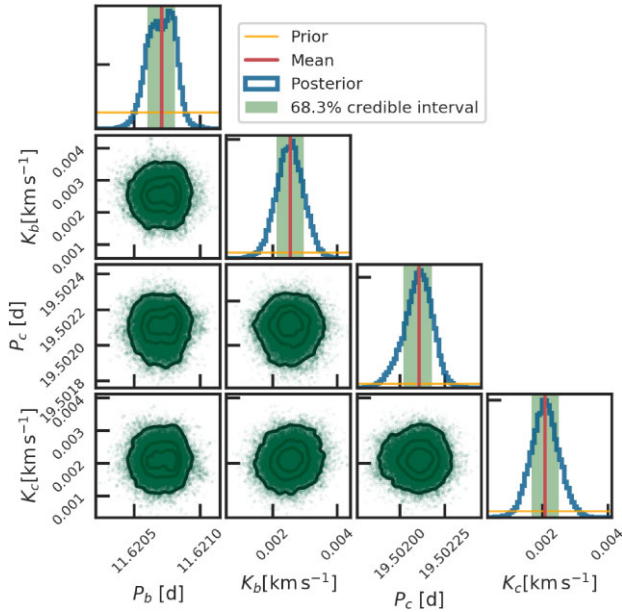
Figure 8. 1D and 2D posterior distributions for the orbital periods and semi-amplitudes of planets b and c from the final MCMC analysis. In the 1D plots on the diagonal, the blue histograms show the distribution of the samples, the red vertical line shows the median, and the green shaded region shows the $\pm 1\sigma$ interval. The horizontal orange line denotes the prior, which for all the parameters shown here was uniform and extends beyond the range of the plots. In the off-diagonal, 2D parameter correlation plots, the green points show the individual samples and the contours show the 68 per cent, 95 per cent, and 99 per cent confidence intervals.

4σ, despite the strong constraints on the orbital ephemerides provided by the transits.

As a final check, we computed the Lomb–Scargle periodogram of the RV residuals, which is shown as the purple line in Fig. 5. There are no significant peaks in the residuals, indicating no detection of additional planets in the system and or periodic signals correlated with our estimated stellar rotation period.

4.5 Planet masses and radii

We used the parameters of the transit and RV fit, reported in Table 3, together with the stellar mass and radius from E21, to derive the bulk and orbital parameters of each planet. These are reported in Table 4. For planet b we find a mass of $9.82^{+1.71}_{-1.61}$ $M_\oplus$ and radius of 3.05 ± 0.11 $R_\oplus$, and for planet c we find a mass of $9.67^{+1.97}_{-1.92}$ $M_\oplus$ and a radius of $5.94^{+0.18}_{-0.16}$ $R_\oplus$.

The masses and radii of the two planets are shown in Fig. 11, where we compare them to published values for other transiting exoplanets from the TEPCAT catalogue (Southworth 2011, sourced 18/9/23). Both planets have very similar masses, but very different radii, and hence densities. While Planet b is a fairly typical sub-Neptune, planet c, by contrast, belongs to the much rarer category of 'superpuffs' – extremely low-density sub-Neptune mass planets. HD 152843 c has a radius many times larger than that of similar-mass planets, and a density of 0.25 g cm^{-3} places it around the rough superpuff upper limit of 0.1 g cm^{-3}. Further, this limit has been made around a sample of much shorter period planets, so given its uniquely long period for such a low density, HD 152843 c earns its place in the superpuff regime.

5 DISCUSSION

Having determined the period, masses, and radii of both planets, we can now explore the implications of our results for the system's formation and evolution history, and the insights it can offer to the 'superpuff' class of exoplanet.

5.1 Formation and evolution

The presence of two planets with such similar masses but different densities, both orbiting relatively close to their host star, is potentially puzzling – did the planets form with similar densities but subsequently evolve differently, or are these differences primordial?

To explore the formation and evolution history of this intriguing system, we ran the MESA PLANET planetary evolution simulation (Owen 2020) to explore the range of possible initial states of planet c. This simulation adapts the MODULES FOR EXPERIMENTS IN STELLAR ASTROPHYSICS (MESA Paxton et al. 2011, 2013, 2015, 2018, 2019; Jermyn et al. 2023) stellar evolution code to include a planetary core of a specified density, and an external flux source to emulate the behaviour of the host star that evolves according to a theoretical model. For this simulation, we use a composite core of $\frac{2}{3}$ silicate and $\frac{1}{3}$ iron, as this reflects an Earth-like composition, consistent with the inferences about sub-Neptune cores (Rogers & Owen 2021). For the flux evolution of the external flux source, we chose an MIST stellar model that most closely represents HD 152843 with a stellar mass of 1.16 $M_\odot$ and metallicity of 0.25.

To determine the possible initial characteristics of planet c, simulations are run over a grid of varying core masses, envelope masses, and amounts of internal heating. Once the models are initialized and settled to a steady state, they are evolved starting at a stellar age of 3 Myr – the time at which it is thought that these types of planets have finished forming and the disc has cleared (Hernández et al. 2007; Mamajek 2009) – to the current estimated age of $\sim$ 4 Gyr. We then select the models that have final radii within 5σ of our solution and compute the likelihood over the grid of core masses, initial envelope mass (expressed as a fraction of the core mass), and internal heating [given in terms of the Kelvin–Helmholtz (KH) time-scale – the time required for the planet to irradiate away the energy equivalent to its thermal energy], given our current estimates of the stellar age and planet mass, radius, and equilibrium temperature. These likelihood contours are shown in Fig. 12. The core mass versus initial envelope mass fraction contours (top panel) shows convergence around a core mass of 6 $M_\oplus$ and envelope mass fraction between 0.8 and 0.9 of the core mass. The other two likelihood contours do not show a clear maxima as the initial KH time-scale is tending to higher and higher values, reaching the fixed upper limit imposed as the highest physically meaningful value of initial kinetic energy for planet formation. These results indicate that the initial heat from formation and stellar irradiation are not sufficient to explain the current properties of HD 152843 c, and that an additional source of heating is required to explain the planet's low density. This is assuming that the relatively large radius for HD 152843 c is not the result of high-altitude haze, as this is not in the scope of these models.

5.2 System dynamics

The ratio of the orbital periods of planets b and c ($P_c/P_b = 1.678220 \pm 1.4e-5$) places these planets within 7 per cent of the 5:3 mean motion resonance (MMR). This is a second-order resonance, meaning it is not as energetically favourable or as common (Lissauer et al. 2011) as a first-order 2:1 or 3:2 resonance. Pan,
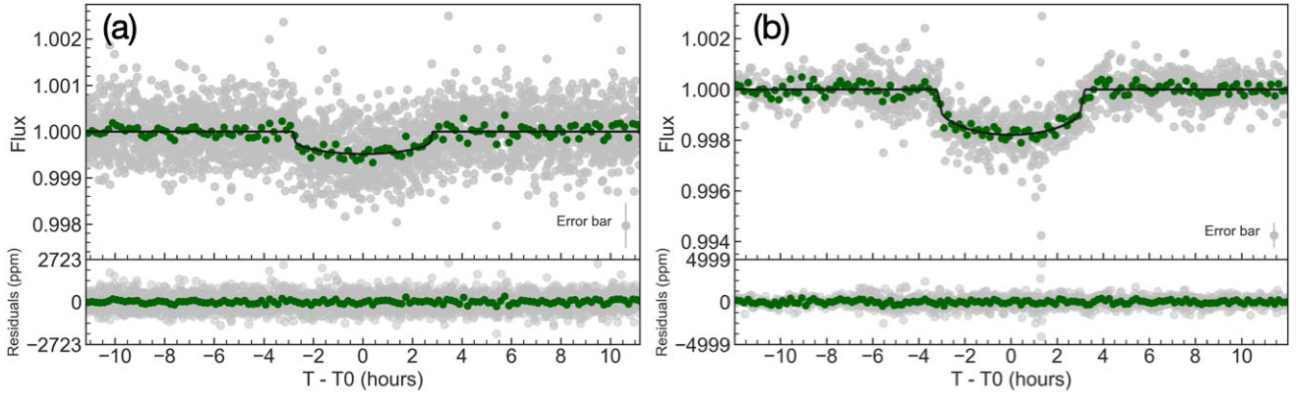
Figure 9. (a) *TESS* light curve phase-folded at the period of planet b, with the best-fitting transit model shown by the black line, and the residuals of this model shown in the bottom panel. The 2-min cadence data used in the fit are shown as grey points, while the green points show the same data binned by a factor of 5 in phase. (b): same for planet c.
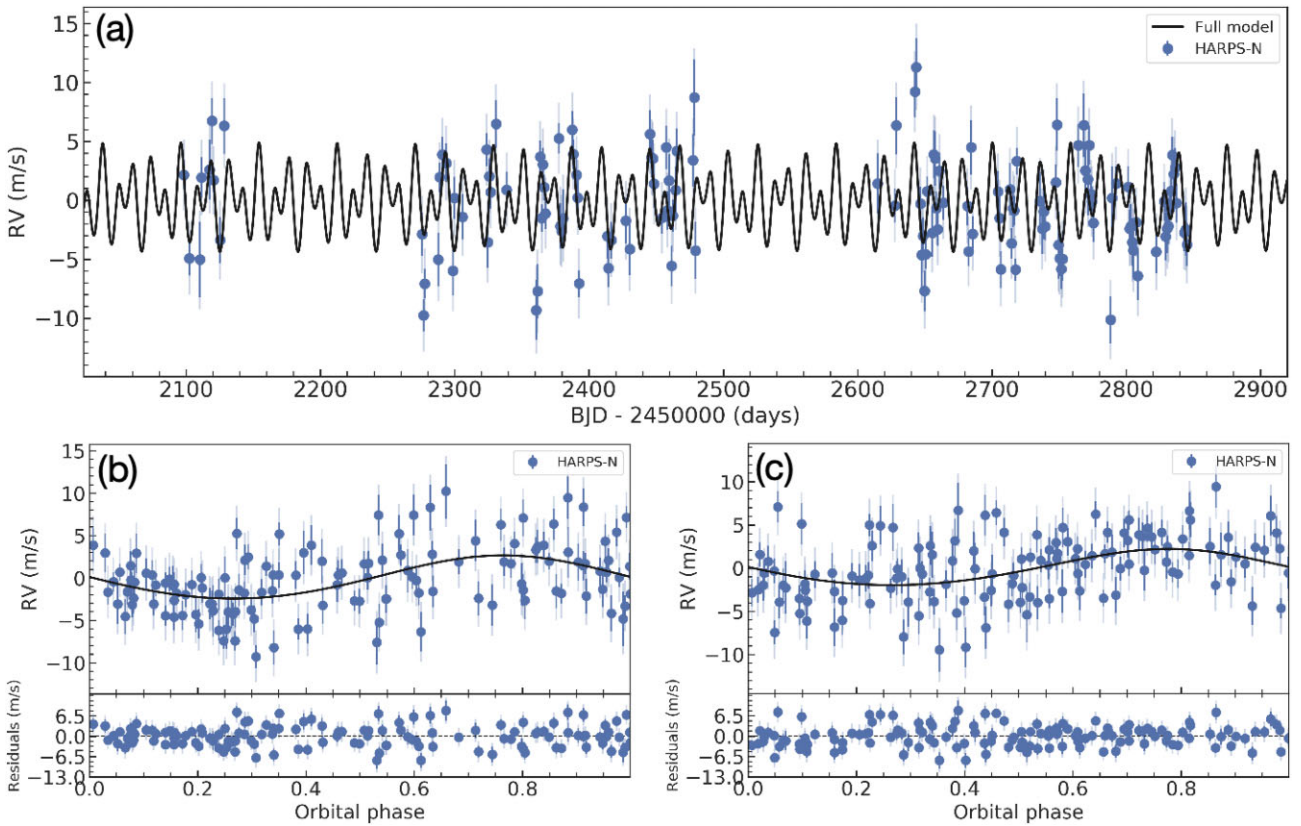

Figure 10. (a) Final fit (black line) to the HARPS-N RVs (blue points). (b) and (c) phase-folded RV curves for planets b and c, respectively, after subtracting the signal from the other planet, with the residuals shown in the lower panel. In all plots, the semitransparent error bars indicate the jitter level added in quadrature to the formal uncertainties.

Wang & Ji (2020) demonstrate that these higher order resonances can occur in systems where two inner planets dynamically interact with an outer giant planet. Further, they showed that a near 5:3 resonance in particular is made possible if the giant planet is on a eccentric orbit. This suggests that there may be, or may have been, a third planet in the HD 152843 system, though no such third planet is seen in the RV or photometric data presented here.

This near MMR may give rise to observable TTVs. The gravitational interactions of *N*-body systems cause them to deviate from Keplerian orbits (Agol et al. 2005; Holman & Murray 2005). This

is detectable in the form of evolving, sinusoidal, periodic offsets in a planet's transit times compared to an average linear ephemeris. These offsets can occur of the order of minutes to hours.

We simulated the expected TTV signal given the planetary system parameters obtained above using the TTVFast package (Deck et al. 2014). Because of the proximity of the planets' periods to an MMR, a periodic signal is expected to be observed with an amplitude of 15–20 min, as seen in Fig. 13, which shows the simulated residuals to a linear ephemeris of each planet over a superperiod. While uncertainties exist on each of the input parameters, Fig. 14 shows a range of

Table 4. Derived system parameters.

| Parameter	Value
Derived parameters HD 152843b	
Planet mass ($M_\oplus$)	$9.82^{+1.71}_{-1.61}$
Planet radius ($R_\oplus$)	3.05 ± 0.11
Planet density ρ (g cm^{-3})	$1.9^{+0.41}_{-0.36}$
Semimajor axis a (au)	$0.1049^{+0.0029}_{-0.003}$
Eccentricity e	$0.046^{+0.058}_{-0.033}$
Transit duration τ (h)	$5.59^{+0.13}_{-0.14}$
Orbit inclination i (deg)	$89.26^{+0.51}_{-0.58}$
Instellation F_p ($F_\oplus$)	$265.4^{+22.1}_{-20.4}$
Derived parameters HD 152843c	
Planet mass ($M_\oplus$)	$9.67^{+1.97}_{-1.92}$
Planet radius ($R_\oplus$)	$5.94^{+0.18}_{-0.16}$
Planet density ρ (g cm^{-3})	$0.253^{+0.059}_{-0.057}$
Eccentricity e	$0.074^{+0.072}_{-0.05}$
semimajor axis a (au)	$0.1482^{+0.0041}_{-0.0042}$
Transit duration τ (h)	$6.5^{+0.16}_{-0.11}$
Orbit inclination i (deg)	$89.21^{+0.53}_{-0.4}$
Instellation F_p ($F_\oplus$)	$133.1^{+11.1}_{-10.2}$
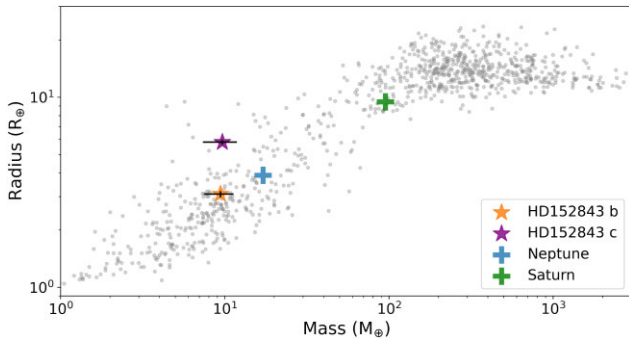
Figure 11. The plot show mass versus radius of HD152843 b and c compared with the sample of known planets with masses and radii known to better than 50 per cent precision, sourced from the TEPCAT data base. For reference, Neptune and Saturn are shown as blue and green pluses, respectively.

TTV amplitudes across a 2σ distribution of input parameters, with the most significant influence coming from planetary masses and eccentricities. As expected, the signal is most sensitive to eccentricity, with higher eccentricities leading to larger TTVs. However, a wide range of masses and eccentricities in the two planets should still allow for TTVs to be detectable, given the precision of individual transit times for each planet of the order of 4 and 2 min for planets b and c, respectively.

The superperiod, P_{TTV}, of two interacting planets in j:j-i orbital resonance is given by

$$P_{\mathrm{TTV}} = \left| \frac{j-i}{P_{\mathrm{inner}}} - \frac{j}{P_{\mathrm{outer}}} \right|^{-1}. \tag{1}$$

For the HD 152843 system, this gives rise to a superperiod of approximately 560 d, which for planet b is of the order of 50 epochs. While the spread in transit times covers this superperiod, several more intermediate transits would be necessary to confirm the non-linearity of residuals.

We checked for any tentative evidence of TTVs in the four transits observed so far for planet b, as follows. We fit each transit
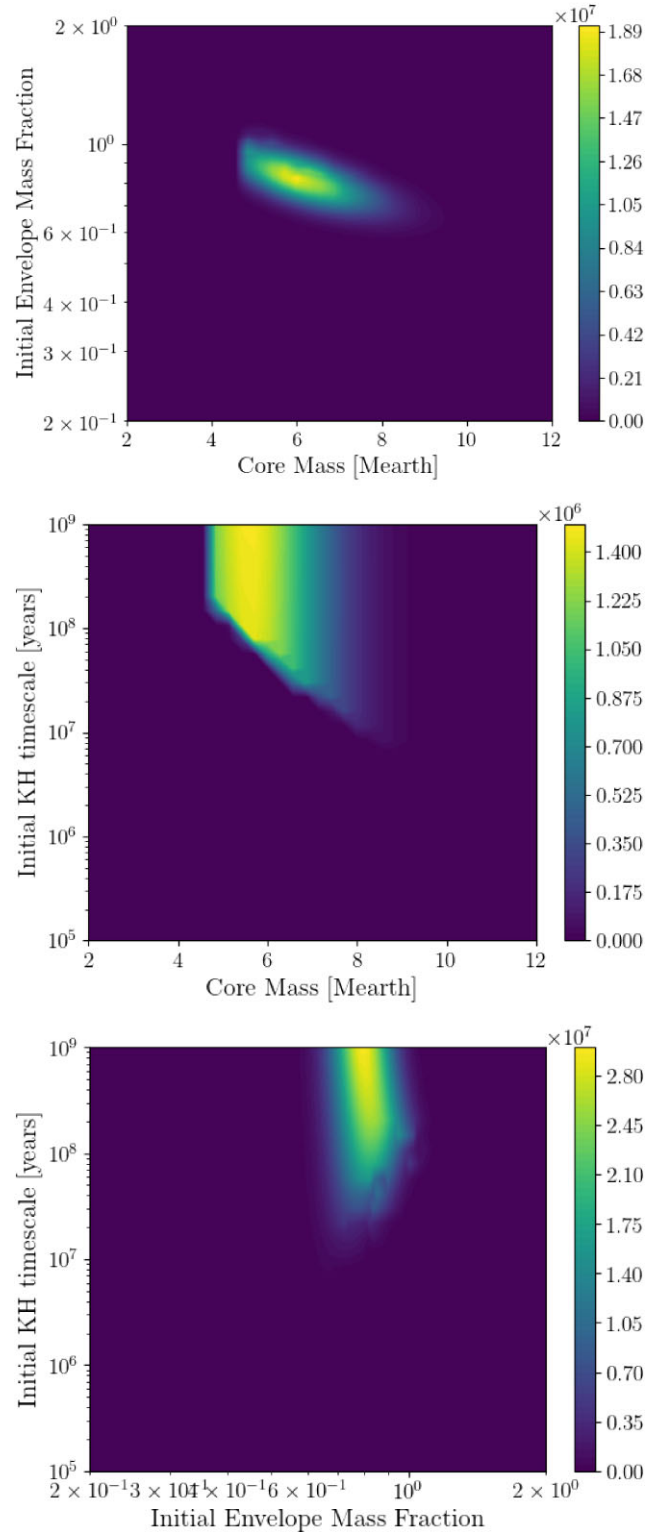

Figure 12. Results of the MESA planet modelling showing the likelihood contours for the three-dimensional parameter space of core mass, initial envelope mass fraction, and initial internal heating (parametrized as the KH cooling time-scale). The lack of a clear, Gaussian-like maximum likelihood, and the tendency of the solution to push to higher and higher KH time-scales beyond values that are physical indicate that the energy from initial formation and stellar irradiation alone is not enough to explain the current measured properties of HD 152843 c.
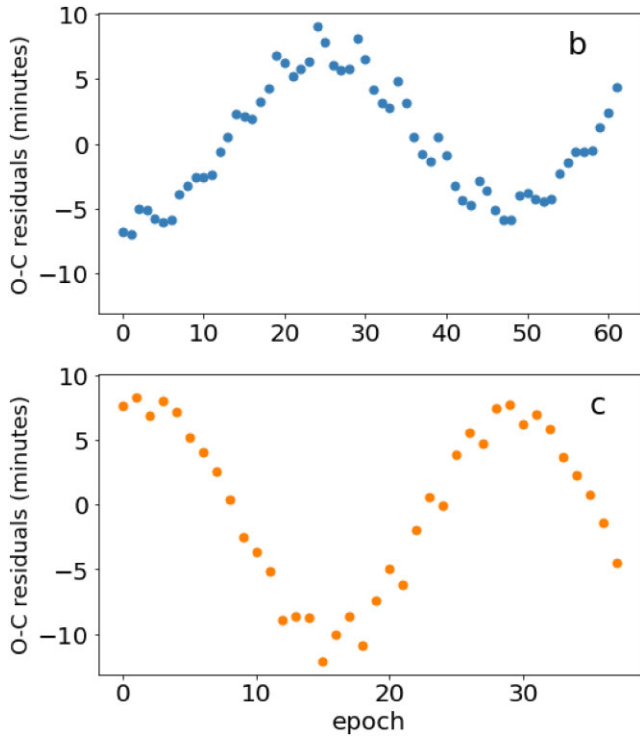
Figure 13. The expected Observed minus Calculated (O-C) residuals for planet b (top) and c (bottom) for planetary parameters obtained in this study, which show periodic TTVs with detectable amplitudes. Significant scatter or 'chopping' of the order of minutes can be seen in the timings of both planets.
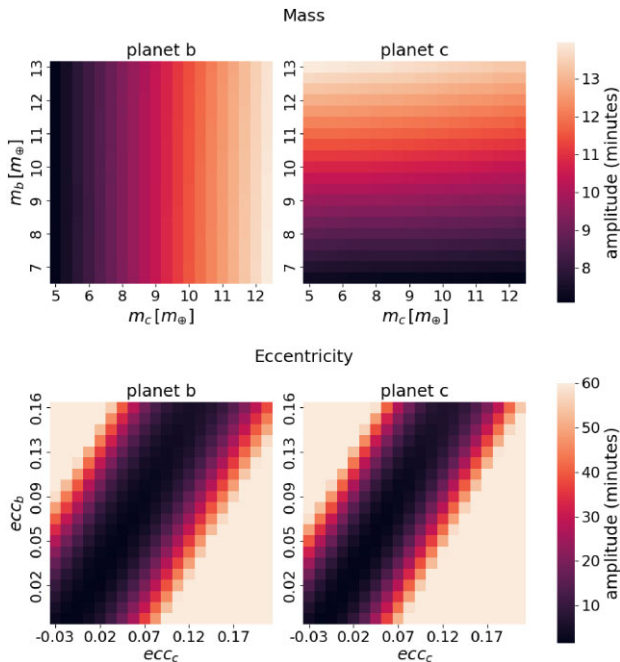

Figure 14. Heatmaps show expected amplitudes of TTVs (O-C offsets) for a range of parameters across our uncertainty distribution. The effect of varying the mass of each planet to 2σ plus or minus is shown in the top panel, and the effect of varying eccentricities is shown in the bottom panel. For most combinations, TTVs remain detectable at amplitudes of 10 min or more. In each case, the parameter in question is varied, while all other parameters are fixed at their median value.
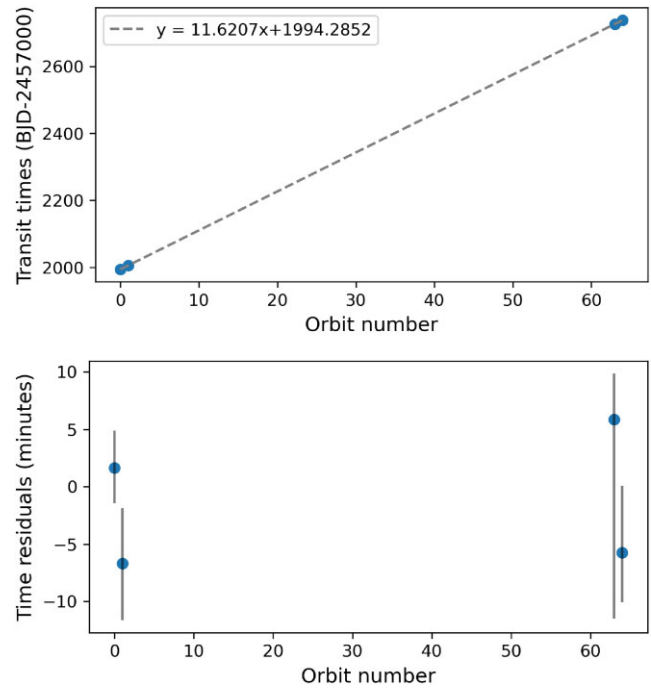

Figure 15. Top panel: transit times of HD 152843 b in *TESS* data as a function of transit number. Bottom panel: residual in transit time compared to a linear ephemeris (perfectly Keplarian orbit). These data show no obvious signs of TTVs; however the scatter in the points in large uncertainties do not rule them out.

individually, keeping all the parameters fixed to the values given in Table 3, and varying only the time of transit centre (T_0). These values are plotted in the top panel of Fig. 15, along with the linear ephemeris determined by out joint fit in Section 4. The transit time residuals from this linear ephemeris are shown in the bottom panel of Fig. 15. There are no TTVs obviously present in these data; however, given the uncertainties of each time point, TTVs are not ruled out. Further, the scatter currently observed in mid-point times of the four transits of planet b is consistent with chopping effects, which are the short time-scale offsets associated with the planet's synodic period evolution (Deck & Agol 2015). More transit observations are needed to confirm the presence of any TTVs and enable us to better constrain planetary masses and orbital properties.

5.3 Prospects for atmospheric characterization

The combination of a bright host star and two Neptune-mass transiting planets makes the HD 152843 system an ideal target for atmospheric studies and comparative planetology. HD 152843 c in particular is an outstanding target for transmission spectroscopy owing to its extremely low density, and has very high transmission spectrum metric (TSM, as defined in Kempton et al. 2018) of 304, and HD 152843 b has a lower TSM of 53. This places planet c well above the threshold TSM of 90 for 'high-quality atmospheric characterization' as defined by Kempton et al. (2018). By measuring the transmission spectra of both planets over an appropriate wavelength range, one could constrain the metallicities and C/O ratios of their atmospheres, and, more importantly, allow us to determine the reason for the large radius of planet c by indicating the presence or lack thereof of high-altitude haze.

To illustrate the observable potential of planets b and c with *JWST*, we computed a suite of forward models using the open-
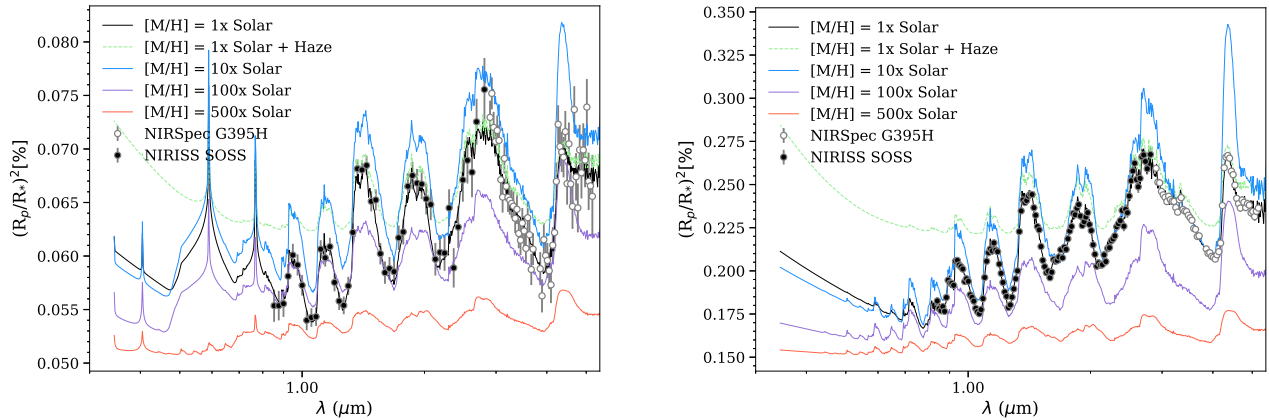
Figure 16. Simulated transmission spectra for planets b (left) and c (right) for different assumptions regarding metallicity and the presence of a haze. The points with error bars show single-transit observations with *JWST* observations simulated using PANDEXO, demonstrating that molecular features would be detected at high confidence irrespective of those assumptions, particularly using the NIRSpec/G395H grism.

source code CHIMERA (Line et al. 2013) and compared these to synthetic observations of each planet that were generated using PANDEXO (Batalha et al. 2019). We use PANDEXO to model a single transmission spectrum of each planet using NIRISS/SOSS and NIRSpec/G395H, thus spanning multiple H_2O bands and important carbon-bearing molecules such as CO_2 and CH_4. We use the newly derived system parameters presented in Table 4. We assume an isothermal temperature structure (values taken from table 1 in E21) and model the atmosphere without clouds. We model the atmospheres to have a solar C/O ratio and metallicities of $1\times$, $10\times$, $100\times$, $300\times$, and $500\times$ solar, respectively. We generated an additional model with haze for our $1\times$ solar metallicity model, to highlight how haze would impact the transmission spectrum. We used the chemical grid developed in Kreidberg et al. (2015). These models can be seen in Fig. 16; we overplot our synthetic observations for the $1\times$ solar metallicity model. The black data points are the synthetic NIRISS/SOSS observations and the white points are the synthetic NIRSpec/G395H data points. It is important to use both of these observing modes as they span key parts of the transmission spectrum. NIRISS/SOSS probes the haziness of the atmosphere; high-altitude hazes would mute the H_2O bands in this region. NIRSpec/G395H spans an H_2O band, CO_2 band, and CH_4 band, thus possible to measure the C/O of the atmosphere.

6 SUMMARY AND CONCLUSIONS

This work presents an intensive campaign of radial velocity observations with HARPS-N to measure the masses of the two transiting planets discovered by citizens around HD 152843. Additional *TESS* data, which have become available since the initial publication of this system, have allowed us to refine the radii estimates and orbital periods of both planets. All derived planet properties are summarized in Table 4.

These mass measurements reveal a fascinating planetary system: a low-density, superpuff outer planet in a likely second-order resonant orbit with a typical Neptune-sized inner planet. Such a system allows us to explore scenarios of formation of superpuff planets, and the properties of planetary systems with planets near higher order MMRs. Modelling the formation and evolution of planet c shows that if the large radius is not due to high-altitude haze, it is unlikely that internal heat from formation and host star irradiation alone is enough

to explain its current size. In such a case, an extra source of heat, such as that caused by dynamical interactions between planet b and c, is needed to explain planet c's inflated radius. Future observations with *JWST* and other space-based instruments will allow us to explore the nature of the atmospheres for both targets and will reveal if planet c's large radius is caused by high-altitude hazes or if something more complex is occurring with this system. Future TTV observations and dynamical modelling of this system will give insight to the possible formation and migration scenarios of this system, and the possibility of a distant third planet in the system not seen in the radial velocity or photometric data to date.

DATA AVAILABILITY

The *TESS* data are publicly available via the Barbara A. Mikulski Archive for Space Telescopes[2] (MAST). The HARPS-N DRS data published here are publicly available via the Data & Analysis Centre for Exoplanets[3] (DACE), and our full table of the DRS and YARARA RVs and data products are available on Vizier CDS after publication. All other data and analysis products used in this paper are available on request.

[2]https://mast.stsci.edu/
[3]https://dace.unige.ch/

REFERENCES

Agol E., Steffen J., Sari R., Clarkson W., 2005, MNRAS, 359, 567
Baranne A. et al., 1996, A&AS, 119, 373
Barragán O., Gandolfi D., Antoniciello G., 2019, MNRAS, 482, 1017
Barragán O., Aigrain S., Rajpaul V. M., Zicher N., 2022, MNRAS, 509, 866
Batalha N. E. et al., 2019, Astrophysics Source Code Library, record ascl:1906.016
Bourrier V. et al., 2021, A&A, 654, A152
Bruntt H. et al., 2010, MNRAS, 405, 1907
Cosentino R. et al., 2012, in McLean I. S., Ramsay S. K., Takami H.eds, Proc. SPIE Conf. Ser. Vol. 8446, Ground-based and Airborne Instrumentation for Astronomy IV. SPIE, Bellingham, p. 84461V
Cosentino R. et al., 2014, in Ramsay S. K., McLean I. S., Takami H.eds, Proc. SPIE Conf. Ser. Vol. 9147, Ground-based and Airborne Instrumentation for Astronomy V. SPIE, Bellingham, p. 91478C
Cretignier M., Dumusque X., Allart R., Pepe F., Lovis C., 2020a, A&A, 633, A76
Cretignier M., Francfort J., Dumusque X., Allart R., Pepe F., 2020b, A&A, 640, A42
Cretignier M., Dumusque X., Hara N. C., Pepe F., 2021, A&A, 653, A43
Deck K., Agol E., 2015, ApJ, 802, 19
Deck K. M., Agol E., Holman M. J., Nesvorný D., 2014, ApJ, 787, 132
Dumusque X. et al., 2021, A&A, 648, A103
Eisner N. L. et al., 2021a, MNRAS, 501, 4669
Eisner N. L. et al., 2021b, MNRAS, 505, 1827
Fausnaugh M. M. et al., 2022, Technical Report, TESS Data Release Notes: Sector 52, DR76. NASA, https://tasoc.dk/docs/release_notes/tess_sector_52_drn76_v01.pdf
Gao P., Zhang X., 2020, ApJ, 890, 93
Gelman A., Rubin D. B., 1992, Stat. Sci., 7, 457
Gelman A., Carlin J., Stern H., Rubin D., 2003, Bayesian Data Analysis, Second Edition. Chapman and Hall/CRC Texts in Statistical Science, Taylor and Francis, Boca Raton, Florida
Hara N. C., Boué G., Laskar J., Correia A. C. M., 2017, MNRAS, 464, 1220
Helled R., 2023, A&A, 675, L8
Hernández J. et al., 2007, ApJ, 671, 1784
Holman M. J., Murray N. W., 2005, Science, 307, 1288
Jenkins J. M. et al., 2016, in Chiozzi G., Guzman J.C., eds, Proc. SPIE Conf. Ser. Vol. 9913, Software and Cyberinfrastructure for Astronomy IV. SPIE, Bellingham, p. 99133E

Jermyn A. S. et al., 2023, ApJS, 265, 15
Jontof-Hutter D., 2019, Annu. Rev. Earth Planet. Sci., 47, 141
Kempton E. M. R. et al., 2018, PASP, 130, 114401
Kipping D. M., Spiegel D. S., Sasselov D. D., 2013, MNRAS, 434, 1883
Kreidberg L. et al., 2015, ApJ, 814, 66
Lammer H. et al., 2016, MNRAS, 461, L62
Lightkurve Collaboration, 2018, Astrophysics Source Code Library, record ascl:1812.013
Line M. R. et al., 2013, ApJ, 775, 137
Lissauer J. J. et al., 2011, ApJS, 197, 8
Mamajek E. E., 2009, in Usuda T., Tamura M., Ishii M.eds, AIP Conf. Proc. Vol. 1158, Exoplanets and Disks: Their Formation and Diversity. Am. Inst. Phys., New York, p. 3
Mandel K., Agol E., 2002, ApJ, 580, L171
Millholland S., Petigura E., Batygin K., 2020, ApJ, 897, 7
Owen J. E., 2020, MNRAS, 498, 5030
Pan M., Wang S., Ji J., 2020, MNRAS, 496, 4688
Paxton B., Bildsten L., Dotter A., Herwig F., Lesaffre P., Timmes F., 2011, ApJS, 192, 3
Paxton B. et al., 2013, ApJS, 208, 4
Paxton B. et al., 2015, ApJS, 220, 15
Paxton B. et al., 2018, ApJS, 234, 34
Paxton B. et al., 2019, ApJS, 243, 10
Ricker G. R. et al., 2015, J. Astron. Telesc. Instrum. Syst., 1, 014003
Rogers J. G., Owen J. E., 2021, MNRAS, 503, 1526
Southworth J., 2011, MNRAS, 417, 2166

SUPPORTING INFORMATION

Supplementary data are available at *MNRAS* online.

suppl_data

Please note: Oxford University Press is not responsible for the content or functionality of any supporting materials supplied by the authors. Any queries (other than missing material) should be directed to the corresponding author for the article.

This paper has been typeset from a TEX/LATEX file prepared by the author.